Commissioning of a Preheat Strategy of a Molten Salt Test Receiver

Isabell Reisch[1][https://orcid.org/0000-0002-7302-6696], Cathy Frantz[1][https://orcid.org/0000-0002-3455-3311]], Marcel Sibum[2][https://orcid.org/0000-0002-5522-9633], Matthias Binder[3], Christian Schuhbauer[3][https://orcid.org/0000-0002-1145-3115], María Fernández-Torrijos[4][https://orcid.org/0000-0001-7834-8240]

[1] German Aerospace Center, Institute of Solar Research, Stuttgart, Germany

[2] German Aerospace Center, Institute of Solar Research, Juelich, Germany

[3] MAN Energy Solutions SE, Germany

[4] Departamento de Ingeniería Térmica y de Fluidos, Universidad Carlos III de Madrid, Leganés (Madrid) Spain

Abstract. Solar power tower plants that are operated with molten salt offer the advantage that the molten salt can be used as a heat transfer medium as well as storage medium. Consequently, solar energy can be stored easily and efficiently in only one loop without transformation losses. Furthermore, by using large-scale storage facilities, almost a 24/7 base load operation is possible. Since the molten salt begin to crystallize at temperature of 238 °C, the absorber tube must be preheated before the plants' operation can begin. During the preheating a subset of heliostats will be aimed on the receiver surface to ensure a solar flux density that leads to tube temperatures above the solar salt crystallization point. Since the absorber tubes are empty during the preheating, there is a risk of high temperature gradients and transients and thus high thermal stresses that may lead to fatigue damage. To prevent this, a preheating strategy for a molten salt test receiver was developed and tested, taking into account ambient conditions and time. The present work shows the results of the commissioning of the developed preheating strategy and discusses its potential for improvement.

Keywords: Solar Salt, CSP, Central Receiver, Solar Preheating, Commissioning, HPMS-II

1. State of the Art

Solar tower power plants with molten salt as heat transfer and storage medium show great potential as solution for the intermittent and fluctuation issues of other renewable energy sources [1]. Base load operation is possible because the molten salt is stored in an insulated tank and is available for power generation for several hours - even in the absence of solar radiation. In order to reduce thermal losses, molten salt receivers are drained at least on a daily basis during periods of low solar resource. Before solar operation is resumed, it must be ensured that all pipes transporting the molten salt are at a temperature level that prevents the molten salt from crystallising. The typical molten salt is molten nitrate salt (sodium nitrate ($NaNO_3$) 60 % wt. and potassium nitrate (KNO_3) 40 % wt.). This salt solidifies at a temperature about 221 °C and starts to freeze at 238 °C [2]. The target temperature of the solar preheating is thus reaching more than 240 °C. Most of the plant's pipes are heated electrically using mineral insulated resistance heaters. However, this approach cannot be used for the receiver' absorber, as they are irradiated with a high solar flux density during solar operation. They are therefore preheated by the solar radiation reflected from the heliostat field. This process is called solar preheating. The difficulty during solar preheating is that the receiver is only filled

with air. Due to the low thermal conductivity of the air, high temperature gradients and transients and thus high thermal stresses can occur between the irradiated and the backside of the tube, which can lead to structural damage [3]. This damage can be prevented by applying a solar preheating strategy. Li et al [4] performed numerical and experimental analyses of a preheating process for a lab-scale receiver in which the tubes of the receiver were heated with xenon lamps, with the aim of producing a non-uniform heat flux distribution. They investigated the preheating process at different heat fluxes and ambient temperatures and compared the results with results from simulations. Pérez-Álvarez et al. [5] studied the non-neglectable influence of different mechanical attachment on the preheating temperature of a central receiver tube. Zuo et al [6] showed the influence of high wind speeds during preheating and determined the preheating duration and the maximum thermal stresses. Vant-Hull [7, 8] developed a preheat algorithm that calculated the solar flux density to be applied as a function of the receiver temperature, with a target receiver temperature of 260 °C. Although the algorithm takes into account the receiver temperature, it does not take into account the occurring temperature gradients and thus also not the occurring thermal stresses. However, subsequent structural mechanical simulations showed that the Vant-Hull algorithm does not compromise the structural integrity of the studied receiver tubes [9]. Another preheat strategy was presented in Reisch et al [10]. This strategy is the subject of this paper and was developed for the MAN Energy Solution test receiver at the DLR Multi Focus Tower in Jülich (Germany). It considers the day of the year, the time, the ambient conditions and a maximum allowable heating rate of 30 K/min. In the following course of the paper, the theoretical background is briefly summarised and finally the results of the commissioning are presented.

2. Theoretical Background

The preheat strategy was developed for the HPMS-II/SALSA molten salt receiver test facility (FIG 1) that is located in the Multi Focus Tower in Jülich Germany. It is a tubular molten salt receiver, manufactured by MAN Energy Solutions, consisting of 16 absorber tubes welded to the header via connecting tubes of the same diameter (TAB 1). The absorber tubes are made of the austenitic steel DMV310 N, which is designed for the use in high temperature areas applications and exposes good corrosion resistance [11]. Apart from the absorber tubes, the receiver is covered with insulation. The engineering of the receiver allows a mass flow range between 1.3 to 12.8 kg/s in serpentine flow and allows the operation at incident solar flux density up to 1000 kW/m² [12].

The preheat strategy was developed based on optical and thermal simulations. From the optical simulation, that were performed with the DLR raytracing program called SPRAY, a relation between the number of focused heliostat and resulting solar flux density is deduced. This relation respects the DNI and the heliostat field performance, that is integrated in the scaling factor R_s. Both of impact factors depend on the elevation θ and azimuth angle γ and hence on the time of the day and the day of the year. Further information about the scaling factor can be found in Reisch et al [10]. In order to achieve a conservative prediction, Clear Sky DNI is assumed in all models. The Clear Sky DNI is calculated based on of the Hottel-Correlation [13]. The results of the optical simulation can be summarized by the following formula:

$$n_{\text{Helio, }\gamma,\theta} = n_{\text{Helio,REF}} \cdot \frac{DNI_{\text{clear Sky, REF}}}{DNI_{\text{clear Sky,}\gamma,\theta}} \cdot \frac{1}{R_s} \cdot \frac{\dot{q}_{\text{SF,GOAL,}\gamma,\theta}}{\dot{q}_{\text{SF,GOAL,REF}}} \tag{1}$$

The number of necessary heliostats $n_{\text{Helio,}\gamma,\theta}$ -in order to achieve a certain incident solar flux density $\dot{q}_{\text{SF,GOAL,}\gamma,\theta}$ at the receiver at a certain elevation and an azimuth is calculated based on reference conditions for which the relation between solar flux and number of necessary heliostats in known. The 21st of June at Solar Noon is chosen as a reference condition. At this time, a $DNI_{\text{clear Sky,REF}}$ of 810 kW/m² requires $n_{\text{Helio,REF}} = 11$ heliostats to generate a flux density $\dot{q}_{\text{SF,GOAL,REF}}$ of 3 kW/m².
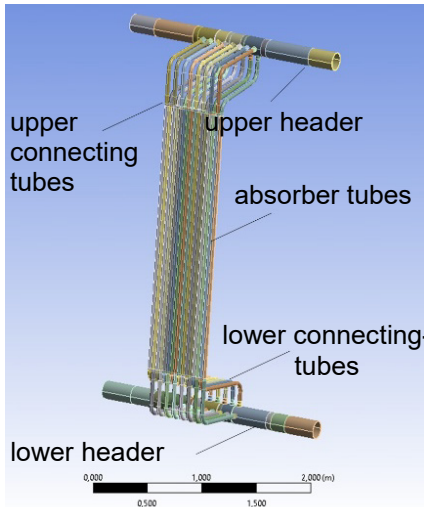
Figure 1. Test Receiver [10].

Table 1. Layout test receiver [10].

Feature	Value
Thermal rating	1 MW$_{th}$
Tube outside diameter	36.8 mm
Maximum incident flux density	1000 kW/m²
Tube wall thickness	2 mm
Absorber tube lengths	2.2 m
Number of absorber tubes	16
Number of serial tubes	8

In a second step, a transient thermal FEM simulation is performed to simulate the necessary solar flux density incident on the receiver surface $\dot{q}_{SF,GOAL,\gamma,\theta}$ in order to maintain a defined heating rate of 30 K/min, specified by the absorber coating manufacturer. The resulting solar flux density is on the one hand a function of the gradient between absorber and ambient temperature and on the other hand a function of the ambient conditions such as wind. The calculated flux density represents the maximum allowable flux density on the receiver so that the temperature ramp of 30 K/min is maintained. By connecting the results of both simulations, the number of heliostats to be focused $n_{\text{Helio},\gamma,\theta}$ can be determined, as a function of the ambient conditions, the receiver temperature and the time of the year, to maintain the temperature ramp of 30 K/min until a target backwall temperature of 290 °C is reached.

3. Experimental Setup

The commissioning of the preheat strategy was part of the commissioning of the High Performance Molten Salt Receiver System in the test facility in Jülich, also called SALSA-Loop that was developed by MAN Energy Solution and DLR. This loop provides the required infrastructure to enable tests at all operation conditions for different receiver prototypes, including solar preheating [14]. The loop consists of salt storage tanks, the salt pump, inlet and outlet vessels, and an automated control system. A steam generator is not a part of the loop, therefore an air cooler is installed to dissipate the thermal energy absorbed by the receiver. More Information about the loop can be found in Frantz et al [12, 14]. To enable the operation of the solar preheating, the temperature of the receiver backside $T_{abs,back}$ is measured by 48 Type K class 1 thermocouples that are uniformly distributed over the absorber height (FIG 2) and the width of the receiver. The temperature on the frontside $T_{abs,front}$ is tracked by an infrared camera, called ImageIR by InfraTec (temperature measuring accuracy with sun shield filter: ±2 K up to 100°C, then ±2 % range full-scale) (FIG 3). The hemispherical absorptance over the solar spectrum of the absorber tubes were measured with the portable measuring device "SOC 410-Solar" and amount of $\alpha = 0,96$ and the hemispherical emissivity over the infrared spectrum was determined by calibration and amount of $\varepsilon = 0,8$ [11]. The solar flux density $\dot{q}_{SF}$ is measured with gardon-type flux gauges (accuracy of ±0,3 %) that are distributed over the height on the left and right side of the receiver edge (FIG 4). Furthermore, the test facility tracks the ambient temperature T_∞ and the wind speed v_w. The measured heating rate of the receiver backside $\Delta T_{trans} = \frac{dT_{abs,back}}{dt}$ is deduced by using the slope of a moving linear fit over a duration of 60s.
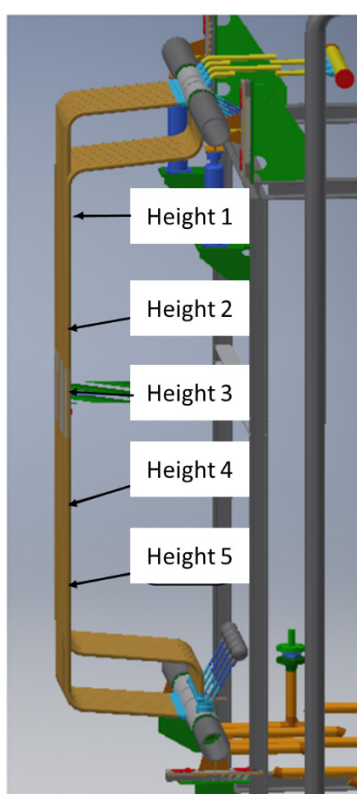
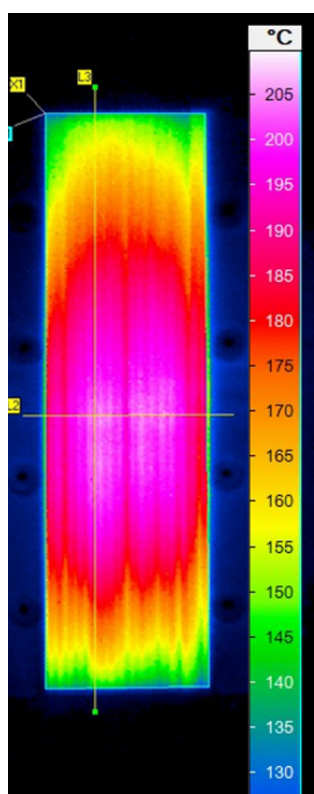**Figure 2.** Thermocouple distribution over absorber tube height.

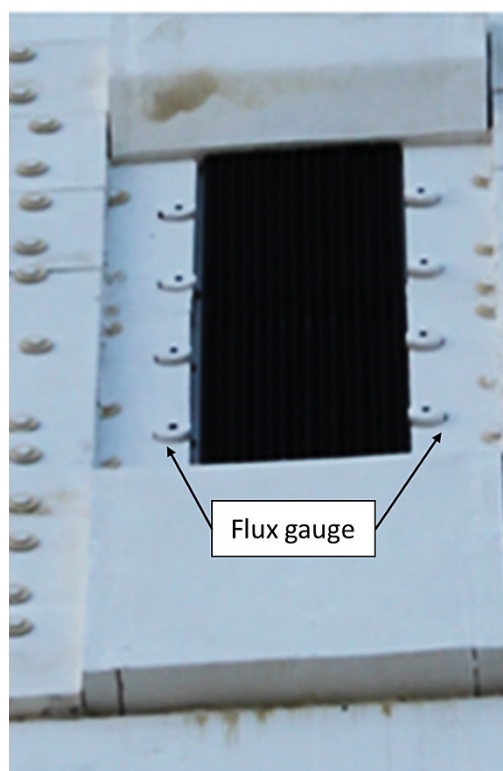**Figure 3.** Temperature distribution measured by IR-Camera.

Figure 4. Position of the 8 Radiometer.

The heliostat field in Jülich has a north field configuration and consist of 1996 heliostats. For the solar preheating only a part of the solar field is needed. During commissioning (which mostly took place in the morning while the sun was in the east), it became apparent that the heliostats in the north or northwest in the background are the best choice, as they produce a large image on the receiver surface.

4. Results of Commissioning compared to the Simulation

The first tests of the commissioning were plausibility tests. The aim was to verify the results from the optical simulation with the real heliostat field performance. The test took place on the 12th of May between 11:30 – 12:00 o'clock local time. During this time, the elevation changes from 43° to 47 ° and the azimuth angle changes from -53° to -43, with a resulting DNI change from 821 W/m² to 841 W/m². The number of heliostats on the receiver surface was increased over time and the maximum solar flux density on the receiver surface was determined by the flux gauges. Optical simulations with the raytracing program SPRAY are carried out to verify the operating data with the simulations. For this purpose, the same boundary conditions (DNI, time and aim points) as in the commissioning experiment are implemented in SPRAY. The solar flux density on the receiver surface was calculated for every increase in number of heliostats. The measured solar flux density data was then compared with the simulated solar flux density data. The results are shown in figure 5.
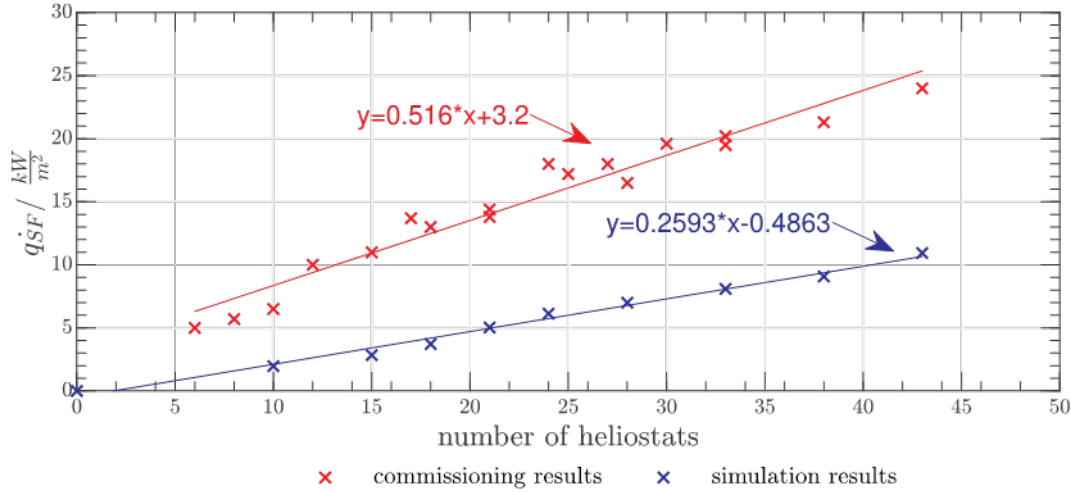
4

Figure 5. Comparison of measured and simulated solar flux-density as a function of the number of focused heliostats.

The red graph shows the measured data, the blue one the simulated data. It can be seen that both of the graphs indicate a linear relationship between the number of heliostat and the solar flux density. However, the graphs show differences in the slope. The graph describing the measured data has a steeper slope than the graph describing the simulated data. Thus, for a given number of heliostats, a higher flux density is achieved under real conditions than assumed in the simulation. This is due to the fact that new heliostats were implemented in the Jülich heliostat field, which expose better performance than the heliostats previously assumed in the simulation. To re-implement this relationship in the calculation, the ratio of the slope of the measured data $slope_{measured}$ to that of the simulated data $slope_{simulated}$ is calculated and added to the formula as a factor:

$$n_{\text{Helio},\gamma,\theta} = n_{\text{Helio, REF}} \cdot \frac{DNI_{\text{clear Sky, REF}}}{DNI_{\text{clear Sky},\gamma,\theta}} \cdot \frac{1}{R_s} \cdot \frac{\dot{q}_{SF,GOAL,\gamma,\theta}}{\dot{q}_{SF,GOAL,REF}} \cdot \frac{slope_{simulated}}{slope_{measured}} \tag{2}$$

This correction enables the correct determination of the number of heliostats that must be focused to reach a certain solar flux density.

The first commissioning tests with one aim point show that the more heliostats are focused, the more inhomogeneous the flux density distribution over the height of the receiver becomes. As a consequence, high temperature gradients over the tube length are observed: the target temperature is achieved in the receiver center, while the areas with lower irradiation remained at temperatures below the crystallization point. As a consequence, it was decided not to work with only one target point in the centre of the receiver, but with 9 target points distributed over the height and width of the receiver. During operation, the operator decides how many heliostats will be focused on which target point.

A further and critical observation was the occurrence of high circumferential temperature differences $\Delta T_{\text{circ}} = T_{\text{abs,front}} - T_{\text{abs,back}}$ above 100 K between the irradiated side and the non-irradiated side during preheating with temperature transients of 20 K/min. As can be seen in Reisch et al [10], the temperature differences are decisive for the thermal stresses occurring in the tubes and for their lifetime. In order not to affect the lifetime of the HPMSII- absorber tubes, the circumferential absorber tube temperature differences ΔT_{circ} should be below 70 K

[10]. Since the maximum temperature difference were exceeded during preheating at a temperature transient of 20 K/min, not only the temperature transients but also the temperature differences ΔT_{circ} are the limiting factors of the preheating.

5. Development of relationship between solar flux density and occurring temperature differences

For the 15th of June, the preheating tests are repeated with the aim to develop a relationship between the maximum allowable flux density incident on the receiver $\dot{q}_{SF,max}$ as a function of occurring temperature differences ΔT_{circ}. Two tests are conducted. The condition for the tests can be found in Table 2.

Table 2. Boundary conditions during preheating tests.

	Preheating at 20K/min	Preheating at 10 K/min
Local Time in Jülich	11:50 to 12:35	13:34 to 14:35
Ambient temperature/ °C	24	26
Wind speed/ m/s	1.5-4.0	0.5-2.7
Target heating rate $\frac{dT_{abs,back}}{dt}$	20 K/min	10 K/min

Figure 6 shows the temperature of the non-irradiated tube backside $T_{abs,back}$ at 42 measurement points and the maximum measured solar flux density $\dot{q}_{SF,max}$ as a function of time for the preheating at 10 K/min. It can be seen that the preheating started at a tube temperature over 50 °C (which is a typical temperature achieved without focusing any heliostats), that the target temperature of 290 °C was reached after approx. 30 min and that the quasi-steady state occurred after approx. 45 min at an average temperature of 310 °C. For the test at 20 K/min the target average temperature of 290 °C was reached after 20 minutes and the quasi-steady state occurred after approx. 35 minutes at an average temperature of 320 °C.
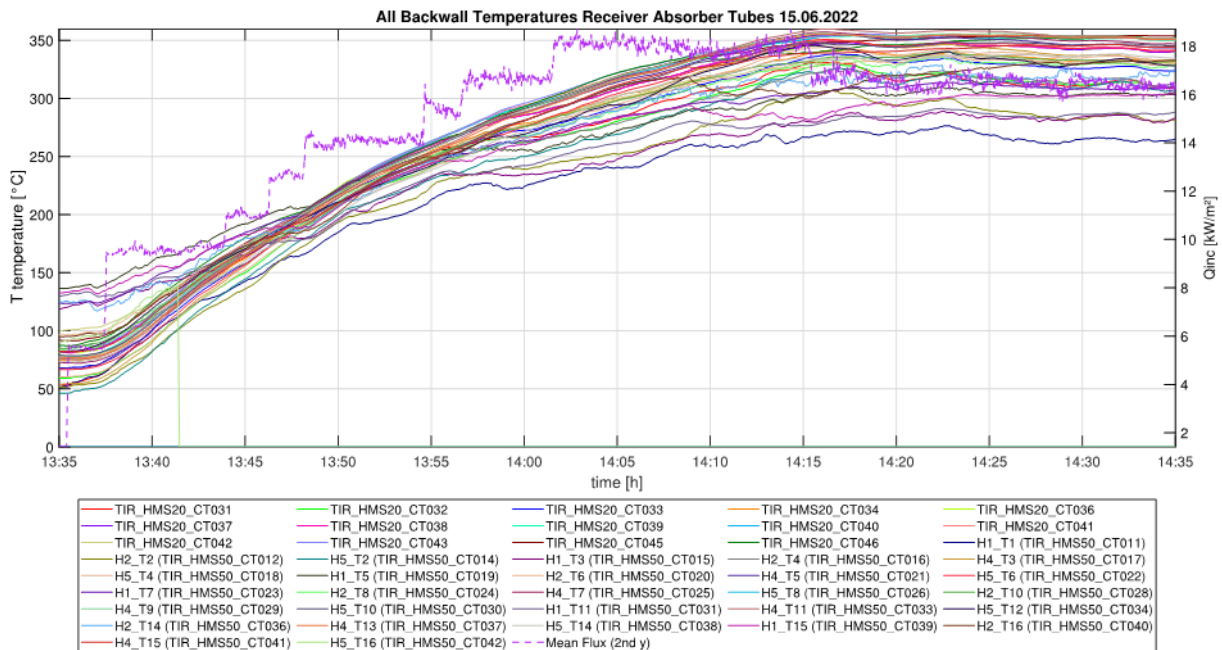

Figure 6. Receiver backwall temperature at 42 measurment points and solar flux density as a function of time at a heating rate of 10 K/min.

The highest circumferential temperature difference ΔT_{circ} occurs at the area where the highest flux density is applied [15]. Therefore, the maximum circumferential temperature difference

$\Delta T_{circ,max}$ and the maximum solar flux density $\dot{q}_{\mathrm{SF,max}}$ as a function of time are evaluated and are shown in figure 7.
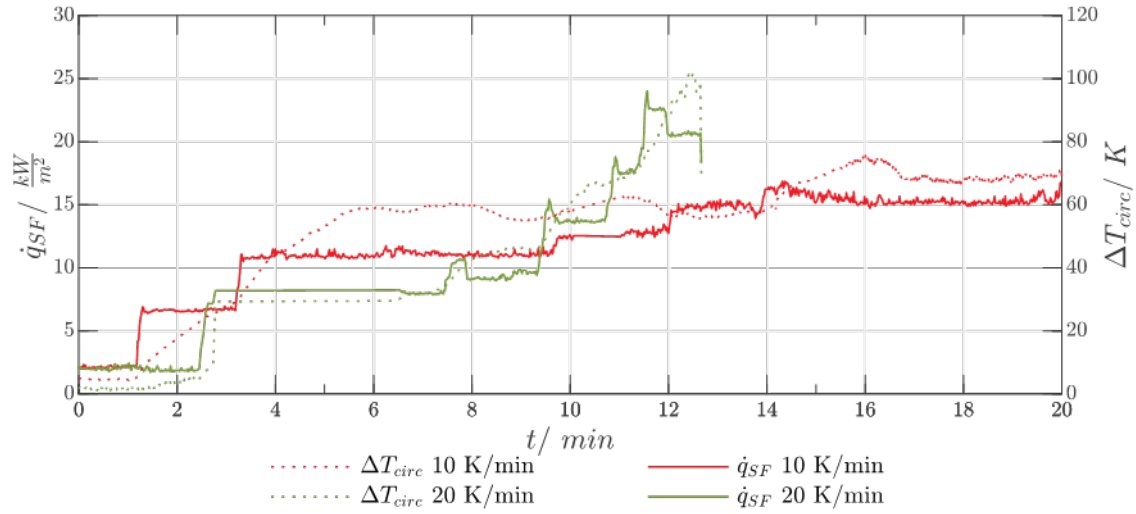

Figure 7. Solar flux density and occurring temperature difference between irradiated and non-irradiated tube side as a function of the time.

The solid lines show the occurring temperature difference ΔT_{circ} and the dotted lines show the maximum solar flux density $\dot{q}_{\mathrm{SF,max}}$- both as a function of time for two different heating rate. It can be seen that during the preheating with a heating rate of 20 K/min, the maximum permissible temperature difference ΔT_{circ} of 70 K are exceeded by large – with maximum temperature differences ΔT_{circ} of 100 K. During preheating with a temperature rate of 10 K/min, the maximum temperature difference ΔT_{circ} were maintained. In order to develop a relationship between the flux density and the temperature differences ΔT_{circ}, the data of the temperature differences were plotted as a function of the flux density (FIG. 8)
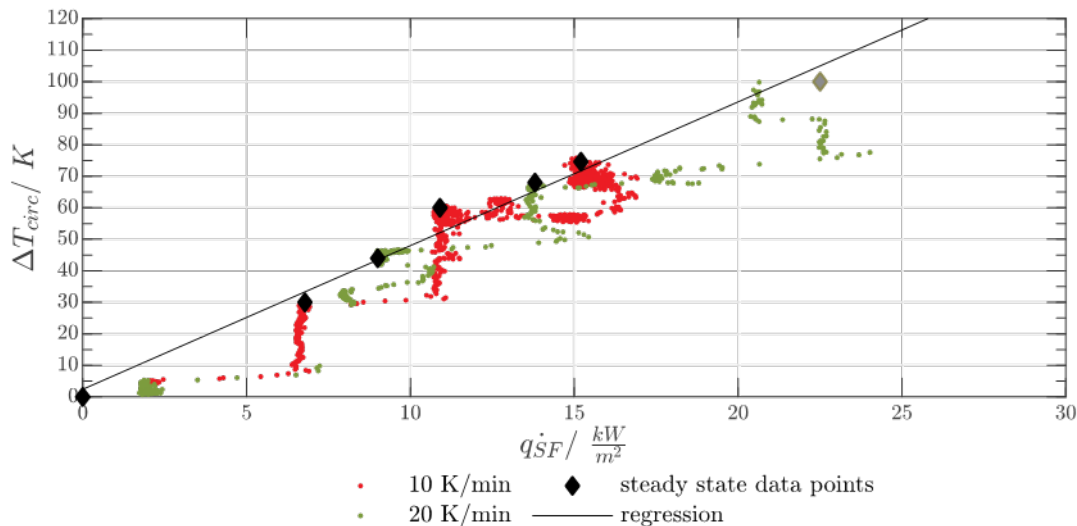

Figure 8. Circumferential temperature difference between the irradiated and non-irradiated tube side as a function of the solar flux density for preheating at 20 K/min and at 10 K/min.

In figure 8 the red dots show the data points for preheating at a heating rate of 10 K/min and the green dots, the data points of preheating at 20 K/min. It can be seen that as the solar flux

density increases, the temperature difference ΔT_{circ} also increases. The vertical clustering of data points at constant flux density is a result of the stepwise change in flux density. When the solar flux density changes significantly in a short time, the temperature differences adjust to the new flux density with a time delay (FIG 7). The result is that the temperature differences change at constant flux density until they reach the steady-state value. It was observed that the highest value of the vertical data accumulation describes the temperature difference that occurs at steady state (marked by black trapezoids). The horizontal course of data point is the consequence of the delay in temperature increase after increase of heat flux.

Figure 7 shows that during preheating at 20 K/min, the flux density increased to about 24 kW/m² and dropped to about 21 kW/m² in a short time. When the flux density dropped to 21 kW/m², the steady state temperature had not yet been reached. This means that the temperature differences of 100 K shown in Figure 8 are not due to the flux density of 21 kW/m², but to the flux density of 24 kW/m² (FIG 8. last grey trapezoid). The stationary points of the temperature differences for the different flux densities are shown as black trapezoids in Figure 8. A proportional relationship between temperature difference and flux density can be observed, which is represented by a regression line. In order not to exceed the temperature differences of 70 K, a maximum flux density of about 16 kW/m² may be aligned. This flux density was sufficient to reach the target backwall temperature of 290 °C.

During operation, it was observed that the faster the flux density was changed, the higher the occurring temperature transients. If the flux density was kept constant for a longer period of time, the temperature transients decreased. Thus, it can be concluded that the temperature transients do not depend on the flux density, but on the change in flux density. Based on these observations, it can be concluded that for solar preheating, the temperature transients of 30 K/min are the limiting factor for the solar flux density increase, but the maximum flux density is limited by the maximum temperature difference ΔT_{circ}. The relationship between the occurring temperature transients and the increase in flux density is still pending and should be developed by using data from future preheating tests.

6. Summary and Outlook

With the results of the commissioning, it was possible to implement the optical real conditions of the heliostat field in Jülich into the preheating strategy. Furthermore, it turned out that by preheating with a temperature transient of 20 K/min, the maximum allowable temperature difference between the irradiated and the non-irradiated side of 70 K is exceeded. This shows that the limiting factor of preheating for test receiver is not only the temperature ramp ΔT_{trans} but also the temperature difference ΔT_{circ}. As a result, a maximum allowable flux density of 16 kW/m² was defined to maintain the maximum allowable temperature difference ΔT_{circ}. From the tests, it is to be expected that the preheating will take approximately 45 minutes. In the next commissioning tests a relationship between the occurring temperature transients and the increase in flux density should be developed and on the basis of these results the preheat strategy should be improved. These results were obtained for the austenitic stainless steel DMV 310 N and an absorber wall thickness of 2 mm. For receivers constructed out of nickel base alloys or exposing lower wall thicknesses, the allowable ΔT_{circ} is higher and the heating rate can be increased.

Author contributions

I. Reisch: Conceptualization, Methodology, Validation, Writing - review & editing
Marcel Sibum: Conceptualization, Methodology, Validation, Writing - review & editing
C. Frantz: Supervision, Conceptualization, Methodology, Validation, Writing - review & editing
Maria Fernandez: Conceptualization, Methodology, Validation, Writing - review & editing

Matthias Binder: Conceptualization, Methodology, Validation, Writing - review & editing
Christian Schuhbauer: Supervision, Review & Editing

Competing interests

"The authors declare no competing interests."

Funding

References

1. A. Boretti. "Realistic expectation of electricity production from current design concentrated solar power solar tower with thermal energy storage", Energy Storage, vol. 1, 2019, https://doi.org/10.1002/est2.57
2. A. Bonk et al., "Solar Salt - Pushing an old material for energy storage to a new limit", Applied Energy, vol. 262, 2020, https://doi.org/10.1016/j.apenergy.2020.114535
3. Du et al, "Analysis of thermal stress and fatigue fracture for the solar tower molten salt receiver", Applied Thermal Engineering, vol. 99, 2016, https://doi.org/10.1016/j.applthermaleng.2016.01.101
4. Y. Li, "Experimental and numerical study on the preheating process of a lab-scale solar molten salt receiver", Renew. Energy, vol. 182, pp. 602-614, 2022, https://doi.org/10.1016/j.renene.2021.10.051
5. R. Pérez-Álvarez et al, "Impact of a mechanical attachment on the preheating temperatures of a central receiver tube", Applied Thermal Engineering, vol. 215, 2022, https://doi.org/10.1016/j.applthermaleng.2022.118854
6. Y. Zuo et al," Numerical study on preheating process of molten salt tower receiver in windy conditions", Energy, vol. 251, 2022, https://doi.org/10.1016/j.energy.2022.123893
7. L.L Vant-Hull, "The Role of "Allowable Flux Density" in the Design and Operation of Molten-Salt Solar Central Receivers", Solar Energy Engineering, vol. 124, 2002, https://doi.org/10.1115/1.1464124
8. L.L Vant-Hull, M.E Izygon and C.L. Pitman, "Real-time computation and control of solar flux density on a central receiver (Solar Two) (preheat)", Solar Engineering, 1996
9. R. Pérez-Álvarez et al, "Thermal stress and fatigue damage of central receiver tubes during their preheating", Applied Thermal Engineering, vol. 195, 2021, https://doi.org/10.1016/j.applthermaleng.2021.117115
10. I. Reisch et al., "Preheat strategy of a molten salt test receiver", Solar Paces, Albuquerque; US, 2021

11. G. Stefano et al, „HPMS - High Performance Molten Salt Tower Receiver System : öffentlicher Schlussbericht : 01.10.2014-31.12.2016", [Deutsches Zentrum für Luft- und Raumfahrt e.V., Institut für Solarforschung]. https://doi.org/10.2314/GBV:1010747207
12. C. Frantz et al., "Basic Engineering of a High Performance Molten Salt Tower Receiver System" (Solar PACES 2020), https://doi.org/10.1063/5.0085895
13. A. Islahi, S. Shakil and M. Hamed, "Hottel's Clear Day Model for a typical arid city- Jeddah" , International Journal of Engineering Science Invention, vol. 4, pp. 32-37, 2015
14. C. Frantz et al., "Commissioning of a Solar Salt Test Setup for Central Receiver Operation at 600 °C" (Solar PACES 2022)
15. Du et al. , "Analysis of thermal stress and fatigue fracture for the solar tower molten salt receiver", Applied Thermal Engineering, vol. 99, Pp. 741-750, 2016, https://doi.org/10.1016/j.applthermaleng.2016.01.101